CrossMark

INVITED PAPER

Paramagnetic defects in hydrothermally grown few-layered MoS_2 nanocrystals

Luis M. Martinez
Department of Physics, The University of Texas at El Paso, El Paso, Texas 79968, USA

Chinnathambi Karthik
Micron School of Materials Science and Engineering, Boise State University, Boise, Idaho 83725, USA

Madhu Kongara
Micron School of Materials Science and Engineering, Boise State University, Boise, Idaho 83725, USA; and Department of Physics, Boise State University, Boise, Idaho 83725, USA

Srinivasa Rao Singamaneni[a)]
Department of Physics, The University of Texas at El Paso, El Paso, Texas 79968, USA

(Received 22 January 2018; accepted 30 April 2018)

In the recent past, two-dimensional (2D) nanocrystalline (NC) transition metal dichalcogenides such as MoS_2 received a great deal of attention due to their extraordinary physical properties. There has been a great interest to study the defects present in MoS_2 NCs, which alter the material's catalytic, electrical, and magnetic properties. This work reports paramagnetic point defects present in the hydrothermally grown 2H–MoS_2 NCs. X-band electron spin resonance (ESR) spectroscopy has been used to identify the defects which contain unpaired electron spins in the as-prepared and Ar-annealed MoS_2 NCs. At least seven ESR signals were detected originating from four inequivalent paramagnetic defect sites such as adsorbed oxygen species, sulfur vacancies, thio-, and oxo-Mo^{5+}. Upon Ar-annealing, most of these defects did not survive, instead conduction ESR signal was observed. This work signifies the importance of employing ESR spectroscopy and broadens the knowledge in identifying the atomic defects in MoS_2 NCs.

I. INTRODUCTION

Among the two-dimensional (2D) materials, transition metal dichalcogenides (TMDs) have attracted great attention due to their unique physical properties that render them numerous potential applications in the fields of catalysis, energy storage, and optoelectronics.[1–10] These are a class of materials with the formula MX_2, where M is a transition metal element (Mo, W, etc.) and X is a chalcogen (S, Se, or Te). These materials form layered structures of the form X–M–X, with the chalcogen atoms in two hexagonal planes separated by a plane of metal atoms through van der Waals interactions. For instance, MoS_2 is a semiconductor with an indirect band gap of ~1.3 eV in the bulk, turning to a direct gap of 1.85 eV in monolayer form. Furthermore, few-layered nanocrystalline (NC) MoS_2 is being widely studied[1–6] for its promising and attractive electrocatalytic properties in the hydrogen evolution reaction due to increasing number of active sites and enhanced intrinsic conductivity, compared to MoS_2 bulk counterparts.

However, the performance of the devices, which incorporate these materials, is strongly determined by the presence of intrinsic and extrinsic defects. For instance, Addou and colleagues have extensively studied the extrinsic defects in natural MoS2 bulk crystals.[11] Most interestingly, intrinsic defects such as sulfur vacancies, molybdenum antisites, and grain boundaries can actually enhance catalytic properties[12–14] and introduce magnetic functionality.[15–17] Although, it has been largely ignored in most of the literature studies, it is critical to identify the grown-in native defects. They can significantly alter physicochemical properties such as many hydrogenation and hydrodesulphurization catalytic processes and even their magnetic properties. Of particular importance, due to the unexpected physical characteristics (such as spin-valley coupling), 2D materials have provided novel platforms in probing the spin interactions with other degrees of freedom of electrons. Thus, incorporating ferromagnetism, either by introducing defects, dopants, or proximity effect in 2D semiconducting materials such as MoS_2 NCs can open doors to applications in the rapidly emerging spintronics field, data storage, and for low power nonvolatile memory applications at room temperature. Hence, it is extremely important to better understand and control the defects at the atomic level that are present in 2D TMD NCs to realize their potential applications.

Several theoretical and experimental efforts[18–21] were made to investigate defects in these TMD NCs. Previous

a)Address all correspondence to this author.
e-mail: srao@utep.edu
DOI: 10.1557/jmr.2018.149

 © Materials Research Society 2018

https://doi.org/10.1557/jmr.2018.149 Published online by Cambridge University Press

researchers have used several techniques such as transmission electron microscopy (TEM), Raman spectroscopy, and scanning tunneling microscopy to characterize the structural defects present in these materials. Unfortunately, these techniques have no capability in atomically identifying the defects, particularly those that are associated with unpaired electron spins. In addition, these techniques have limited sampling volume, and they tend to introduce artifacts. Among all, the main drawbacks of the TEM imaging technique are an increased possibility of damaging the delicate 2D material and much complex sample preparation processes. On the other hand, electron spin resonance (ESR) spectroscopy probes the entire sample volume, and it is nondestructive. It is an exclusive technique of choice in atomically identifying the paramagnetic spin species in advanced semiconducting materials, compared to other bulk techniques.[22–30] Previously, one of us (Singamaneni) has demonstrated[24–29] the power of ESR spectroscopy in atomically identifying the paramagnetic point defects and impurities present in graphene-derived materials and carbon nanotubes, not accessible by other techniques.

As early as 30–40 years ago, ESR spectroscopy was extensively used[31–35] to understand the relationship between paramagnetic active defect sites and their catalytic performance in a wide range of bulk MoS_2-supported materials. There are few initial reports published[28–30] on the ESR studies of polycrystalline MoS_2 thin films, nanotubes, and fullerene-like structures prepared through gas phase synthesis. These studies have uncovered grain boundary paramagnetic point defects such as sulfur antisite defects and paramagnetic dangling bonds. While these studies are encouraging, to date, there has been no in-detailed work reported that investigates the paramagnetic point defects using the ESR technique, particularly on hydrothermally grown MoS_2 NCs, which will broaden the current knowledge and understanding in elucidating the nature of defects in 2D materials, in general. Hydrothermal method is the commonly used synthesis method in laboratories to prepare catalytic materials at large scale. During the catalytic reactions, the intermediate reaction products are formed, which contain unpaired electron spins. ESR is the ideal experimental probe to identify such paramagnetic centers and their environment, which are catalytically and magnetically active.

This paper reports four distinct paramagnetic point defects that occur in hydrothermally grown MoS_2 NCs. The crystallinity, morphology, phase formation, and valence states of the elements were investigated using X-ray diffraction (XRD), TEM, Raman spectroscopy, and X-ray photoelectron spectroscopy (XPS), respectively. At cryogenic temperatures, X-band (~9.43 GHz) ESR spectroscopy was used to identify the paramagnetic spin species in the as-prepared MoS_2 and Ar-annealed NCs. Measured at 7 K, on the as-prepared MoS_2 NCs, at least seven ESR signals were detected which are associated with g_1 = 2.1144, g_2 = 2.0300, g_3 = 1.9863, g_4 = 1.9417, g_5 = 1.8984, and g_6 = 1.8541, and g_7 = 1.8146. These centers were assigned to adsorbed oxygen species, sulfur vacancies, thio-, and oxo-Mo^{5+}-related defects, respectively.

II. EXPERIMENTAL METHODS

MoS_2 NCs were prepared using a most common facile, bottom-up "hydrothermal method".[14,15,36,37] Hydrothermal method is a flexible, scalable, and widely used approach in preparing the freestanding nanoscale (nanosheets and nanowires) 2D chalcogenide materials and their doped (Co, Cu, and Mn) counterparts. For instance, Zhang[16] and co-authors have prepared MoS_2 nanosheets using the hydrothermal method.

Unlike other "top-down" approaches (chemical exfoliation, sonication of bulk MoS_2, electro-Fenton processing, etc.), this route does not employ harsh synthesis conditions, and expensive and hazardous chemicals. In addition, the yield is higher and is a fast route. Previously, this method was successfully used[38,39] in preparing NC magnetic oxide nanowires by one of us (Singamaneni). All the precursors were used as purchased from Alfa-Aeser without further purification. To describe the procedure briefly, in a typical synthesis method, 0.4 g of Na_2MoO_4–$2H_2O$ was dissolved in 30 mL distilled water under sonication for 20 min (At this step, the desired metal precursor is added). Then 0.38 g of dibenzyl disulfide was added to the solution along with 30 mL of ethanol and sonicated for 30 min. The solution was then transferred into a 100 mL Teflon-lined stainless steel autoclave and was maintained at 250 °C for 18 h. Then the reaction system was allowed to cool down to room temperature naturally. The obtained products were collected by centrifugation and washed with deionized water. Then the stoichiometric MoS_2 NCs were filtered and left to dry over night at room temperature in vacuum. Using this approach, a series of samples including 10% Co, Ni, and Mn-doped MoS_2 NCs have been prepared. However, in this work, the discussion is restricted only to undoped MoS_2 NCs.

An automated Bruker D8 Advance X-ray diffractometer (Bruker, Billerica, Massachusetts) was used in the θ–2θ configuration with the Cu K_α X-ray radiation. The mean crystallite size was estimated using the Scherrer equation. TEM specimens were prepared by dispersing the powders on holey carbon grids. TEM studies were carried out using a JEOL JEM 2100 HR (JEOL Ltd., Tokyo, Japan) operated at 200 kV. XPS were collected on a Physical Electronics Versa probe using microfocused monochromatic Al K_α X-ray (1486.7 eV) source with a pass energy of 23.5 eV at a 45° take-off angle. The X-ray source spot size was about 100 μm and the spectral resolution was 0.2 eV. Spectra from the MoS_2 samples were charge corrected by shifting the recorded scans to adventitious carbon (C1*s*) peak at 284.4 eV. The nature

https://doi.org/10.1557/jmr.2018.149 Published online by Cambridge University Press

of occurring paramagnetic structural point defects was assessed by low temperature (7–40 K) ESR spectroscopy. ESR data were recorded on a Bruker EMX Plus X-band (~9.43 GHz) ESR spectrometer (Bruker, Billerica, Massachusetts), equipped with a high sensitivity probe head. A ColdEdge™ ER 4112HV In-Cavity Cryo-Free VT system (ColdEdge Technologies, Allentown, Pennsylvania) connected with an Oxford temperature controller (Oxford Instruments, Abingdon, United Kingdom) was used for low temperature measurements at 7 K. The complete system was operated by Bruker Xenon software (Billerica, Massachusetts). In addition, all ESR experimental settings were kept constant for reproducibility and consistency. ESR settings: microwave frequency ~9.365 GHz, microwave power = 3.17 mW, modulation amplitude = 2 G (peak-to-peak), modulation frequency = 100 kHz, number of scans = 5, and time constant = 5 ms. Apart from Ar annealing (ultrahigh purity, 4 h, 300 °C) of MoS_2 nanocrystals, it should be noted that the samples studied here were not deliberately exposed to oxygen ambient but were handled under normal ambience. For all ESR measurements, the samples were sealed in a quartz tube under air.

III. RESULTS AND DISCUSSION

To verify the crystal structure of MoS_2 NCs, XRD was used. Figure 1(a) shows the powder XRD pattern of MoS_2 NCs, which can be indexed to hexagonal MoS_2 (PDF 73-1508). Four main peaks are observed at 14, 33, 40, and 59° corresponding to the (002), (100), (103), and (110) planes for MoS_2 NCs, respectively.[15,16] The broad peak appeared at 25° is found to arise from the glass holder used for placing MoS_2 NCs for XRD measurements. Ojha et al. reported[40] a similar XRD pattern for MoS_2 NCs synthesized by the hydrothermal process. The peak broadening clearly shows the NC nature of MoS_2. The Scherrer formula, $D_{hkl} = k\lambda/\beta_{hkl} \cos\theta$, was used to estimate the crystallite size of MoS_2. Here, k is a coefficient ($k = 0.9$), β_{hkl} is the full-width-at-half maximum of the (002) peak, and λ is the wave length ($\lambda = 1.5405$ Å). The calculated crystallite size from XRD line broadening is of 10 nm.

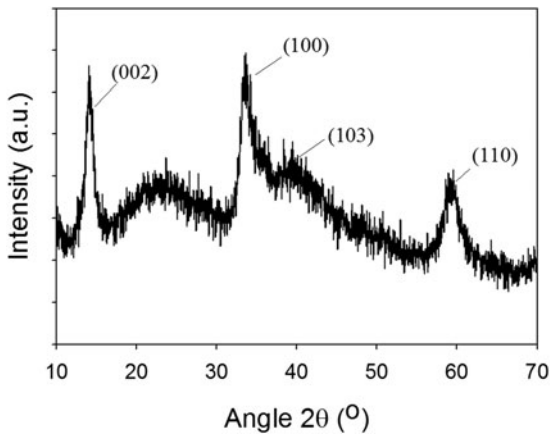


FIG. 1. XRD pattern of MoS_2 nanocrystallites.

Morphological studies were conducted using TEM. Figures 2(a) and 2(b) show the low magnification bright field and the high resolution lattice images, respectively. The indexed selected area diffraction pattern (SAED) is shown as the inset to the bright field image. As can be seen in Fig. 2(b), the MoS_2 NCs (size of 25–30 nm) show the hexagonal structures made up of a few layers of MoS_2 basal planes. The apparent difference in the sizes estimated from XRD and TEM might be because XRD measures crystallite size whereas the TEM shows the grain size. The SAED pattern shown as the inset to Fig. 2(a) contains rings with uniform intensity—confirmed the NC nature of the material. The interlayer spacing measured from the lattice images is 6.45 Å, consistent with the previous reports[1–6] (6.3 Å) of monolayer MoS_2 grown by the CVD methods, and it corresponds to the (002) planes of MoS_2.

XPS survey spectra of MoS_2 NCs indicate the presence of peaks with binding energies (BEs) consistent with molybdenum and sulfur elements besides a lower intensity oxygen and carbon. Absence of other elements demonstrates the purity of the sample. To further probe the chemical composition and surface chemistry, high-resolution core-level XPS spectra were collected on the selected BE intervals. The BE positions were referenced and adjusted to adventitious carbon because of the charging effects on the sample. Shirley method background signal was subtracted and BE peaks were curve-fitted (deconvolution) using Gaussian/Lorentzian functions. Multiple BEs associated with C1*s* spectra are observed at 284.4, 286.3, and 287.9 eV which are assigned to adventitious carbon and C–O impurities from the hydrothermal process. The O1*s* spectral region peak appearing at 532.6 eV is assigned to C–O bonding while the lower BE peak at 530.8 eV is ascribed to Mo–O bonding. The deconvoluted Mo3*d* region had multiple peaks observed at 228.9 (Mo3$d_{5/2}$), 229.9 (Mo3$d_{5/2}$), and 232.48 (Mo3$d_{5/2}$) and their corresponding spin–orbit splitting doublet peaks were noticed at 232.08 (Mo3$d_{3/2}$), 233.1 (Mo3$d_{3/2}$), and 235.6 (Mo3$d_{3/2}$) respectively. In addition, the peak observed at 226.3 eV was assigned to S2s. Spin–orbit split peak separation is found to be around 3.16 eV, which is consistent with the existing literature.[41–43] The peaks corresponding to the S $2p_{3/2}$ and S $2p_{1/2}$ orbital of divalent sulfide ions (S^{2-}) are observed at 161.8 and 162.98 eV associated with another set of deconvoluted peaks appearing at 163.6 and 164.8 eV with an estimated spin–orbit splitting of 1.18 eV. Multiple BE peaks observed in this sample are apparently indicating different phases. The high intensity peak at 228.9 eV (Mo3$d_{5/2}$) resulting from the Mo^{4+} oxidation state is ascribed to the MoS_2 phase[41] with the corresponding S2$p_{3/2}$ 161.8 eV. In addition, the BE peak at 229.9 (Mo3$d_{5/2}$) is associated with higher oxidation

https://doi.org/10.1557/jmr.2018.149 Published online by Cambridge University Press

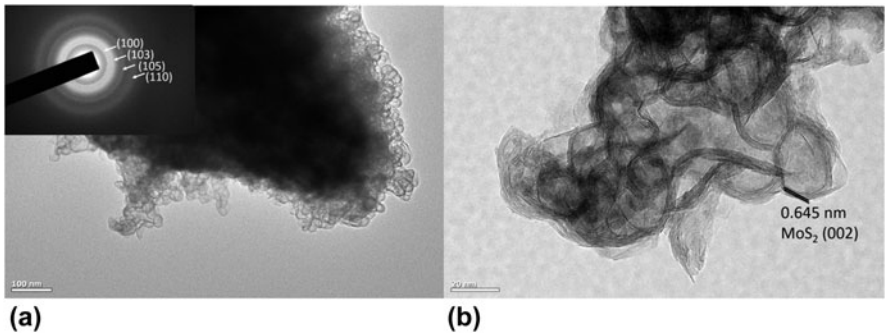


FIG. 2. (a) Bright field TEM image of MoS_2 nanocrystallites. The inset shows the SAED patterns confirming the NC nature of the material. (b) High resolution transmission electron microscopy image of MoS_2 nanocrystallites. The spacing between the layers along the (002) plane is about 0.645 nm.

state molybdenum, along with a secondary peak that corresponds to S2$p_{3/2}$ (161.8 eV) ascribed to the MoS_3 phase.[42] Furthermore, the BE peak at 232.48 eV (Mo3$d_{5/2}$) relating to the higher oxidation state of Mo^{6+} in conjunction with O1s (530.8 eV) is attributed to a mostly stable MoO_3 phase.[43] XPS technique could be used to quantify the ratio of different phases within a given sample. Based on the deconvoluted Mo3d peaks, it is estimated that there is about 65% MoS_2 phase and the remaining is a combination of MoS_3 and MoO_3.

Raman spectrum was used to confirm the few-layered MoS_2 NCs. Raman spectra measured on MoS_2 NCs showed two distinct characteristic[44] peaks at 384 and 408 cm^{-1}, which are associated with the in-plane vibrational (E^1_{2g}) and the out-of-plane vibrational (A_{1g}) modes of Mo–S bonds in 2H–MoS_2, respectively. The Raman peaks are in agreement with that of MoS_2 bulk crystals.

Figure 3 presents an overview of the representative first derivative X-band ESR spectrum measured at 7 K. The spectrum exhibits a wealth of information pertaining to intrinsic paramagnetic spin centers. To authors' knowledge, this is the first single richest spectrum reported to date on any MoS_2 NCs and amorphous/less-crystalline compounds. ESR spectral parameters provide characteristic signatures of paramagnetic defects by analyzing the signal position, width, and shape. From this spectrum, at least seven well-resolved ESR lines are identified, marked from 1 to 7. Only those peaks that are clearly observable are indicated. Since the signals show considerable overlap, it is difficult to determine the ESR parameters of each signal accurately. Nevertheless, within experimental accuracy, the g-values of all the well-resolved peaks and their peak-to-peak line widths that could be detected separately are tabulated in Tables I and II, respectively. The g-values were determined using the resonance condition $h\nu = g\beta H$, where h = Planck's constant, ν = microwave frequency, g = g-value, β = Bohr magneton, and H = resonance field (measured at the turning points). Collected at 7 K, on the as-prepared

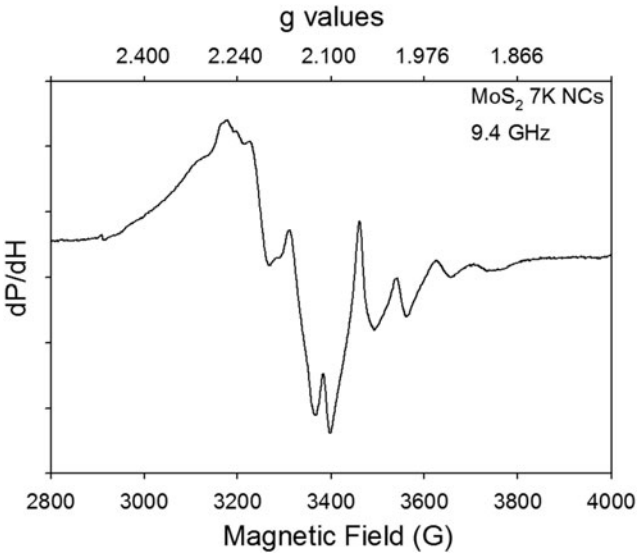


FIG. 3. First-derivative representative X-band (9.40 GHz) ESR spectra measured on MoS_2 nanocrystals at 7 K. One can see that there are at least seven well-resolved ESR lines as marked from 1 to 7. The spectrum is plotted on both the magnetic field and g-value axes.

MoS_2 NCs, at least seven ESR signals are detected, associated with g_1 = 2.1144, g_2 = 2.0300, g_3 = 1.9863, g_4 = 1.9417, g_5 = 1.8984, g_6 = 1.8541, and g_7 = 1.8146. No half-field lines were detected that might correspond to electron spin >1/2. This infers that, most likely, the signals that are observed in the present work arise from spin 1/2 paramagnetic spin centers. Although it has been intensely searched for, no hyperfine interaction originating from ^{33}S (nuclear spin I = 3/2; 0.75% abundance) and ^{95}Mo and ^{97}Mo (both I = 5/2; 25.5% added abundance) could be traced. No external impurities[45–47] from MoS_2 NCs are observed. In addition, as verified from the controlled measurements, no similarity between the ESR spectra measured on MoS_2 NCs and ESR spectra recorded from sulfur and Mo precursors could be found, which clarifies that the unreacted compound could not account for the observed ESR

https://doi.org/10.1557/jmr.2018.149 Published online by Cambridge University Press

spectra. It has been observed that the ESR spectra do not resemble to the spectra collected from the Teflon tape, quartz tube, and empty cavity. In the absence of relevant ESR literature studies, some of the low intense overlapping ESR peaks appeared on the low magnetic field side could not be identified with certainity. Further high frequency ESR spectroscopic measurements in collaboration with National High Magnetic Field Laboratory (NHMFL) Electron Magnetic Resonance (EMR) facility at Florida will be performed in resolving the overlapping ESR signals.

The attention will be paid on the well-resolved ESR signals. To better understand the behavior of observed paramagnetic centers, temperature-dependent ESR measurements (7–40 K) were performed on the as-prepared MoS_2 NCs. The data are presented in Fig. 4. As presented in Tables I and II, the *g*-values and the linewidths of all the ESR signals did not vary significantly as a function of temperature (7–40 K). This observation is consistent with the previous reports[48,49] in support of Mo^{5+} species (discussed later), whose ESR spectra were shown to be temperature-independent. This leads us to believe that these are isolated intrinsic paramagnetic defects and do not interact with each other.

TABLE I. Temperature dependences of *g*-values.

	g values			
`	7 K	10 K	20 K	40 K
Signal 1	2.1144	2.1152	2.1144	2.1136
Signal 2	2.03	2.03	2.03	2.0298
Signal 3	1.9863	1.9867	1.9867	1.9863
Signal 4	1.9417	1.9423	1.9421	1.9421
Signal 5	1.8984	1.8988	1.8988	1.8984
Signal 6	1.8541	1.8545	1.8538	1.8556
Signal 7	1.8146	1.8153	1.8167	1.8131

TABLE II. Temperature dependences linewidths.

	Linewidths			
	7 K	10 K	20 K	40 K
Signal 1	91.3	92.62	89.54	86.24
Signal 2	57.42	56.32	58.3	56.76
Signal 3	14.74	14.08	15.62	14.74
Signal 4	63.36	62.92	62.26	64.9
Signal 5	47.96	47.3	46.86	46.2
Signal 6	62.26	63.8	62.26	62.26
Signal 7	47.96	46.64	45.1	51.26

Annealing MoS_2 NCs under Ar ambience can improve the crystallinity and phase formation, but, at the expense of grain growth. The number of ESR signals decreased due to the decrease in the surface area of MoS_2 NCs as a result of Ar annealing (4 h, 300 °C). Now, the modification of ESR spectra upon post Ar annealing will be considered. Because of Ar annealing, very distinct paramagnetic centers are found. Interestingly, the rich ESR spectrum observed from MoS_2 NCs disappeared. Instead, as presented in Fig. 5, a broad signal (*g*-value = 2.0895; peak-to-peak line width = 821 G) and a narrow signal (*g*-value = 1.9289; peak-to-peak line width = 69 G) are noticed. Upon closer inspection, there are few more weak unresolved narrow signals overriding the broader signal were also detected. This implies that the paramagnetic defect sites observed from pristine MoS_2 NCs still exist, however, with much reduced defect density.

Now, the possible origin of these paramagnetic defect centers involved in the observed ESR spectra will be discussed. The signals in the low field region (<3000 G) are very weak in intensity, also not well resolved compared to the rest of the spectra. Hence, that part of the spectra is excluded from the present discussion. Therefore, the efforts will be focused in analyzing the ESR signals numbered from 1 to 7 in the spectra. Although Mo^{6+} is detected in XPS spectra, it is diamagnetic; not expected[49] to give ESR signal, and hence this

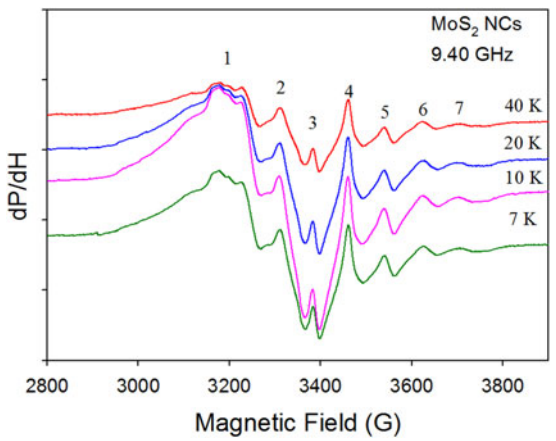


FIG. 4. Temperature dependence (7–40 K) of ESR spectra measured on MoS_2 nanocrystals.

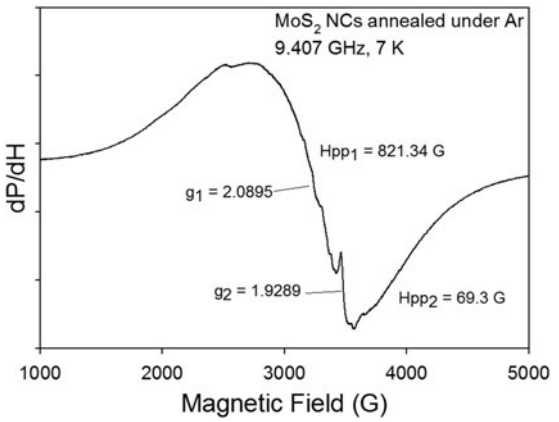


FIG. 5. ESR spectra collected on Ar-annealed (4 h, 300 °C) MoS_2 nanocrystals measured at 7 K.

https://doi.org/10.1557/jmr.2018.149 Published online by Cambridge University Press

possibility can be ruled out. Even it is paramagnetic and abundant as can be seen from XPS, Mo^{4+} would give a quite broad signal due to large zero field splitting. This possibility can also be ruled out as all the signals that are observed have relatively narrower line widths ranging from 40 to 95 G. Mo^{3+} is relatively unstable and cannot be captured using X-band ESR. Hence, Mo^{5+} is the only ion, which is paramagnetic, ESR-detectable, and highly stable. In this work, no attempt was made to derive the absolute spin concentrations of all these paramagnetic defect sites, as it is not straightforward to estimate, particularly, given the strong overlapping of the signals. This might require simulation of entire powder spectra that needs usage of much computational work and modeling,[33,34] which is beyond the scope of the present work.

Previous ESR studies reported[33,34] on MoS_2 compounds will help in identifying the ESR signals observed in the present work. These authors collected ESR spectra when (amorphous/less crystalline) MoS_2 was exposed to water, oxygen, and by varying the S to Mo ratio. Part of the spectra observed in the present work resembles to the previous work reported by Zanchetta's group.[33,34] Their work identified three classes of paramagnetic spin centers with variable intensity, whose ESR signals are of Lorentzian in character. In addition, the previous ESR studies[31,33,35] documented on the bulk MoS_2 supported (Al_2O_3 and SiO_2) catalysts will also assist here in correctly interpreting the spectra. From the analysis presented here together with the help of literature reports,[31–35,50] the signal appeared at $g = 2.1144$ was assigned to oxygen adsorbed species (as measurements were performed in open air), though it was not observed in most of the previous studies.[31–35] The signal appeared at the g-value of 2.0300 was assigned to sulfur chains in MoS_2 NCs. This is consistent with the previous observations reported[33] on irradiated amorphous sulfur, where the electron hole is localized on the sulfur atom. It can be noted this signal is much narrower than that (120–150 G) of the similar sulfur-related signals reported in the literature.[32–35] Perhaps, this might be due to the strong exchange narrowing effect. The ESR signals appeared at $g = 1.9863$, $g = 1.9417$ could come from Mo^{5+} ($4d^1$ configuration) paramagnetic centers surrounded by sulfur-rich environment (MoS_3). The ESR observations appeared at $g = 1.8984$, 1.8541, and 1.8146 could be ascribed to Mo^{5+} paramagnetic centers surrounded by oxygen-rich environment (MoO_3).

Now, ESR spectra of Ar-annealed MoS_2 NCs will be analyzed. The ESR signals are shown in Fig. 5. To trace the origin of the broad signal, the work done[30] by Arcon and co-authors will help us. The authors conducted X-band ESR study on Li-doped MoS_2 nanotubes. They observed two quite different components. A broad (800–2600 G) signal associated with the g-value of 2.15–2.52 and a narrow (~4 G) signal appeared at the g-value of 2.0029 were detected. The g-value of the broad signal is farther from the free electron g-value (2.0023) which suggests the effect of strong spin–orbit coupling from Mo. The authors attributed the broad signal to (d-band in Mo) conduction electrons coupled to defects through exchange interaction. As the g-value and line width of the broad signal observed in the present work are in close agreement with their observations, the broad signal observed in the present work could be assigned to the conduction electron spins. It is natural to expect a similar situation that might have occurred in the current MoS_2 NCs during the Ar annealing process. This results in significant surface reorganization toward bulk-like structure, and, hence, MoS_2 becomes more conducting at the expense of reduction in defect density. On the other hand, the narrower and much weaker signal could be assigned to oxo-Mo^{5+} centers, which might be present in the form of small spin clusters. It is evident that this particular oxo-Mo^{5+} site still survived even after the Ar annealing treatment. This finding implies that the observed spin centers are of surface-related, and probably they are located on the edges of the layers. The spectra remain unaffected even at further higher measurement temperatures (25 and 40 K).

Some of the paramagnetic centers such as sulfur vacancies and Mo-related defects are known to be catalytically active. One can harness them to improve the materials' catalytic performance. As discussed previously, the XRD pattern did not show any evidence of MoS_3/MoO_3 residual phases. However, from the current experimental findings derived from ESR spectroscopy, it is believed that MoS_2 NCs do contain unavoidable MoS_3 and MoO_3 fractions. This observation is consistent with the XPS data as well, where the presence of MoS_3 and MoO_3 fractions was evident. These defects can be exploited for their magnetic and catalytic properties. In fact, the initial magnetic measurements performed on MoS_2 NCs have revealed the presence of ferromagnetism at room temperature. Future work will look into the simulation of the observed X-band ESR spectra and perform very high frequency ESR measurements MoS_2 NCs to gain further insights.

IV. CONCLUSIONS

The paramagnetic spin sites occurred in the hydrothermally grown 2H–MoS_2 nanocrystals were studied. The crystallinity, morphology, phase formation, and valence state were investigated using XRD, TEM, Raman spectroscopy, and XPS, respectively. X-band (~9.43 GHz) ESR spectroscopy was used to identify the paramagnetic point defects in the as-prepared and Ar-annealed MoS_2 nanocrystals, as a function of measurement temperature (7–40 K). From MoS_2 nanocrystals, at least seven ESR

https://doi.org/10.1557/jmr.2018.149 Published online by Cambridge University Press

signals associated with $g_1 = 2.1144$, $g_2 = 2.0300$, $g_3 = 1.9863$, $g_4 = 1.9417$, $g_5 = 1.8984$, $g_6 = 1.8541$, and $g_7 = 1.8146$ were observed. The corresponding peak-to-peak line widths are 91, 57, 15, 63, 48, 62, and 48 G, respectively. These centers were assigned to adsorbed oxygen species ($g = 2.1144$), sulfur vacancies ($g = 2.0300$), thio- ($g = 1.9863$, 1.9417), and oxo-Mo^{5+} ($g_6 = 1.8541$, and $g_7 = 1.8146$) related defects. This work demonstrates the importance of employing ESR spectroscopy in elucidating the paramagnetic (defect) spin states that might have direct correlation in improving the catalytic performance and induce magnetism in advanced semiconducting materials and devices.

ACKNOWLEDGMENTS

L.M.M and S.R.S acknowledge support from a UTEP start-up grant. L.M.M acknowledges the Wiemer Family for awarding Student Endowment for Excellence. S.R.S acknowledges the NSF-PREM program (DMR-1205302). The authors sincerely thank Prof. Russell Chianelli for shared synthesis facilities and for useful discussion. KMR acknowledges the NSF-MRI grant DMR-0722699. C.K. acknowledges the Boise State Center for Materials Characterization (BSCMC) and NSF MRI Grant DMR-0521315. The authors thank S. R.J. Hennadige and E. Castro for their help in performing ESR and Raman spectroscopy measurements, respectively.

REFERENCES

1. J. Kibsgaard, Z. Chen, B.N. Reinecke, and T.F. Jaramillo: Engineering the surface structure of MoS_2 to preferentially expose active edge sites for electrocatalysis. *Nat. Mater.* **11**, 963 (2012).
2. T.F. Jaramillo, K.P. Jørgensen, J. Bonde, J.H. Nielsen, S. Horch, and I. Chorkendorff: Identification of active edge sites for electrochemical H_2 evolution from MoS_2 nanocatalysts. *Science* **317**, 100 (2007).
3. Y. Yu, S-Y. Huang, Y. Li, S.N. Steinmann, W. Yang, and L. Cao: Layer-dependent electrocatalysis of MoS_2 for hydrogen evolution. *Nano Lett.* **14**, 553 (2014).
4. B. Hinnemann, P.G. Moses, J.L. Bonde, K.P. Jørgensen, J.H. Nielsen, S. Horch, I. Chorkendorff, and J.K. Nørskov: Biomimetic hydrogen evolution: MoS_2 nanoparticles as catalyst for hydrogen evolution. *J. Am. Chem. Soc.* **127**, 5308 (2005).
5. H. Wang, C. Tsai, D. Kong, K. Chan, F. Abild-Pedersen, J.K. Nørskov, and Y. Cui: Transition-metal doped edge sites in vertically aligned MoS_2 catalysts for enhanced hydrogen evolution. *Nano Res.* **8**, 566 (2015).
6. G. Liu, A.W. Robertson, M.M-J. Li, W.C.H. Kuo, M.T. Darby, M.H. Muhieddine, Y-C. Lin, K. Suenaga, M. Stamatakis, J.H. Warner, and S.C.E. Tsang: MoS_2 monolayer catalyst doped with isolated Co atoms for the hydrodeoxygenation reaction. *Nat. Chem.* **9**, 810 (2017).
7. K.F. Mak, K. He, C. Lee, G.H. Lee, J. Hone, T.F. Heinz, and J. Shan: Tightly bound trions in monolayer MoS_2. *Nat. Mater.* **12**, 207 (2013).
8. J. Feng, X. Qian, C-W. Huang, and J. Li: Strain-engineered artificial atom as a broad-spectrum solar energy funnel. *Nat. Photon.* **6**, 866 (2012).
9. J.P. Wilcoxon, P.P. Newcomer, and G.A. Samaraa: Synthesis and optical properties of MoS_2 and isomorphous nanoclusters in the quantum confinement regime. *J. Appl. Phys.* **81**, 7934 (1997).
10. J.W. Park, H. Seob So, S. Kim, S-H. Choi, H. Lee, J. Lee, C. Lee, and Y. Kim: Optical properties of large-area ultrathin MoS_2 films: Evolution from a single layer to multilayers. *J. Appl. Phys.* **116**, 183509 (2014).
11. R. Addou, S. McDonnell, D. Barrera, Z. Guo, A. Azcatl, J. Wang, H. Zhu, C.L. Hinkle, M. Q-Lopez, H.N. Alshareef, L. Colombo, J.W.P. Hsu, and R.M. Wallace: Impurities and Electronic Property Variations of Natural MoS_2 Crystal Surfaces. *ACS Nano* **9**, 9124 (2015).
12. C. Tsai, F.A. Pedersen, and J.K. Nørskov: Tuning the MoS_2 edge-site activity for hydrogen evolution via support interactions. *Nano Lett.* **14**, 1381–1387 (2014).
13. G. Li, D. Zhang, Q. Qiao, Y. Yu, D. Peterson, A. Zafar, R. Kumar, S. Curtarolo, F. Hunte, S. Shannon, Y. Zhu, W. Yang, and L. Cao: All the catalytic active sites of MoS_2 for hydrogen evolution. *J. Am. Chem. Soc.* **138**, 16632 (2016).
14. Y. Yin, J. Han, Y. Zhang, X. Zhang, P. Xu, Q. Yuan, L. Samad, X. Wang, Y. Wang, Z. Zhang, P. Zhang, X. Cao, B. Song, and S. Jin: Contributions of phase, sulfur vacancies, and edges to the hydrogen evolution reaction catalytic activity of porous molybdenum disulfide nanosheets. *J. Am. Chem. Soc.* **138**, 79657 (2016).
15. D. Gao, M. Si, J. Li, J. Zhang, Z. Zhang, Z. Yang, and D. Xue: Ferromagnetism in freestanding MoS_2 nanosheets. *Nanoscale Res. Lett.* **8**, 129 (2013).
16. R. Zhang, Y. Li, J. Qi, and D. Gao: Ferromagnetism in ultrathin MoS_2 nanosheets: From amorphous to crystalline. *Nanoscale Res. Lett.* **9**, 586 (2014).
17. L. Cai, J. He, Q. Liu, T. Yao, L. Chen, W. Yan, F. Hu, Y. Jiang, Y. Zhao, T. Hu, Z. Sun, and S. Wei: Vacancy-induced ferromagnetism of MoS_2 nanosheets. *J. Am. Chem. Soc.* **137**, 2622 (2015).
18. S-C. Lu and J-P. Leburton: Electronic structures of defects and magnetic impurities in MoS_2 monolayers. *Nanoscale Res. Lett.* **9**, 676 (2014).
19. A. Azizi, Y. Wang, Z. Lin, K. Wang, A.L. Elias, M. Terrones, V.H. Crespi, and N. Alem: Spontaneous formation of atomically thin stripes in transition metal dichalcogenide monolayers. *Nano Lett.* **16**, 6982 (2016).
20. A. Azizi, S. Eichfeld, G. Geschwind, K. Zhang, B. Jiang, D. Mukherjee, L. Hossain, A.F. Piasecki, B. Kabius, J.A. Robinson, and N. Alem: Freestanding van der Waals heterostructures of graphene and transition metal dichalcogenides. *ACS Nano* **9**, 4882 (2015).
21. J. Hong, C. Jin, J. Yuan, and Z. Zhang: Atomic defects in two-dimensional materials: From single-atom spectroscopy to functionalities in opto-/electronics, nanomagnetism, and catalysis. *Adv. Mater.* **29**, 1606434 (2017).
22. S.S. Rao, A. Stesmans, J.V. Novyen, P. Jacobs, and B. Sels: ESR investigations of ultra-small double walled carbon nanotubes embedded in zeolite nanochannels. *J. Phys.: Condens. Matter* **23**, 455801 (2011).
23. S.S. Rao, A. Stesmans, K. Keunen, D.V. Kosynkin, A. Higginbotham, and J.M. Tour: Unzipped graphene nanoribbons as 'sensitive O_2 sensors'—Electron spin resonance probing and dissociation kinetics. *Appl. Phys. Lett.* **98**, 083116 (2011).
24. S.S. Rao, A. Stesmans, J. van Tol, D.V. Kosynkin, and J.M. Tour: Magnetic defects in chemically converted graphene nanoribbons: Electron spin resonance investigation. *AIP Adv.* **4**, 047104 (2014).
25. S.S. Rao, A. Stesmans, J. van Tol, D.V. Kosynkin, A. Higginbotham-Duque, W. Lu, A. Sinitskii, and J.M. Tour:

https://doi.org/10.1557/jmr.2018.149 Published online by Cambridge University Press

Spin dynamics and relaxation in graphene nanoribbons: Electron spin resonance probing. *ACS Nano* **6**, 7615 (2012).
26. S.S. Rao, S. Narayana Jammalamadaka, A. Stesmans, V.V. Moshchalkov, J. van Tol, D.V. Kosynkin, A. Higginbotham, and J.M. Tour: Ferromagnetism in graphene nanoribbons: Split versus oxidative unzipped ribbons. *Nano Lett.* **12**, 1210 (2012).
27. S.R. Singamaneni, J. van Tol, R. Ye, and J.M. Tour: Intrinsic and extrinsic defects in a family of coal-derived graphene quantum dots. *Appl. Phys. Lett.* **107**, 212402 (2015).
28. A.M. Panich, A.I. Shames, R. Rosentsveig, and R. Tenne: A magnetic resonance study of MoS_2 fullerene-like nanoparticles. *J. Phys.: Condens. Matter*, **21**, 395301 (2009).
29. A. Stesmans, S. Iacovo, D. Chiappe, I. Radu, C. Huyghebaert, S. De Gendt, and V.V. Afanas'ev: Paramagnetic intrinsic defects in polycrystalline large-area 2D MoS_2 films grown on SiO_2 by Mo sulfurization. *Nanoscale Res. Lett.* **12**, 283 (2017).
30. D. Arcon, A. Zorko, P. Cevc, A. Mrzel, M. Remškar, R. Dominko, M. Gaberšček, and D. Mihailovic: Electron spin resonance of doped chalcogenide nanotubes. *Phys. Rev. B* **67**, 125423 (2003).
31. K.C. Khulber, S. Mann, and M. Ternan: Electron spin resonance studies of the surface chemistry of molybdenum-alumina catalysts. *Can. J. Chem.* **56**, 1769 (1978).
32. B.G. Silbernagel, T.A. Pecoraro, and R.R. Chianelli: Electron spin resonance of supported and unsupported molybdenum hydrotreating catalysts. *J. Catal.* **78**, 380 (1982).
33. Y. Bensimon, P. Belougne, J.C. Giuntini, and J.V. Zanchetta: Electron spin resonance of water adsorption on amorphous molybdenum sulfide. *J. Phys. Chem.* **88**, 2754 (1984).
34. B. Deroide, Y. Bensimon, P. Belougne, and J.V. Zanchetta: Lineshapes of ESR signals and the nature of paramagnetic species in amorphous molybdenum sulfides. *J. Phys. Chem. Solids* **52**, 853 (1991); *J. Non-Cryst Solids* **149**, 218 (1992).
35. C. Louis and M. Che: EPR investigation of the coordination sphere of Mo^{5+} ions on thermally reduced silica-supported molybdenum catalysts prepared by the grafting method. *J. Phys. Chem.* **91**, 2875 (1987).
36. W. Gu, Y. Yan, C. Zhang, C. Ding, and Y. Xian: One-Step Synthesis of Water-Soluble MoS_2 Quantum Dots via a Hydrothermal Method as a Fluorescent Probe for Hyaluronidase Detection, *ACS Appl. Mater. Interfaces*, **8**, 11272–11279 (2016).
37. X. Liang, X. Zhang, W. Liu, D. Tang, B. Zhang, and G. Ji, A simple hydrothermal process to grow MoS_2 nanosheets with excellent dielectric loss and microwave absorption performance, *J. Mater. Chem. C* **4**, 6816–6821 (2016).
38. S.S. Rao, K.N. Anuradha, S. Sarangi, and S.V. Bhat: Weakening of charge order and anti ferromagnetic to ferromagnetic switch over in $Pr_{0.5}Ca_{0.5}MnO_3$ nanowires. *Appl. Phys. Lett.* **87**, 182503 (2005).
39. K.N. Anuradha, S.S. Rao, and S.V. Bhat: Complete melting of charge order in hydrothermally grown $Pr_{0.57}Ca_{0.41}$ $Ba_{0.02}MnO_3$ nanowires. *J. Nanosci. Nanotechnol.* **7**, 1775 (2007).
40. K. Ojha, S. Saha, S. Banerjee, and A.K. Ganguli: Efficient electrocatalytic hydrogen evolution from MoS_2-functionalized Mo_2N nanostructures. *ACS Appl. Mater. Interfaces* **9**, 19455 (2017).
41. P.A. Spevack and N.S. Mclntyre: A Raman and XPS investigation of supported molybdenum oxide thin films. 2. Reactions with hydrogen sulfide. *J. Phys. Chem.* **97**, 11031 (1993).
42. W. Zhang, T. Zhou, J. Zheng, J. Hong, Y. Pan, and R. Xu: Water-soluble MoS_3 nanoparticles for photocatalytic H2 evolution. *ChemSusChem* **8**, 1464 (2015).
43. P.A. Spevack and N.S. Mclntyre: A Raman and XPS investigation of supported molybdenum oxide thin films. 1. Calcination and reduction studies. *J. Phys. Chem.* **97**, 11020 (1993).
44. D. Chiappe, I. Asselberghs, S. Sutar, S. Iacovo, V. Afanas'ev, A. Stesmans, Y. Balaji, L. Peters, M. Heyne, M. Mannarino, W. Vandervorst, S. Sayan, C. Huyghebaert, M. Caymax, M. Heyns, S. De Gendt, I. Radu, and A. Thean: Controlled sulfurization process for the synthesis of large area MoS_2 films and MoS_2/WS_2 heterostructures. *Adv. Mater. Interfaces* **3**, 1500635 (2016).
45. J.W.C. Spackman: Electron spin resonance of charge carriers in impure molybdenum disulphide. *Nature* **198**, 1266 (1963).
46. F.D. Brand, G.M. Ribeiro, P.H. Vaz, J.C. González, and K. Krambrock: Identification of rhenium donors and sulfur vacancy acceptors in layered MoS_2 bulk samples. *J. Appl. Phys.* **119**, 235701 (2016).
47. A. Stesmans, S. Iacovo, and V.V. Afanas'ev: ESR study of p-type natural 2H-polytype MoS_2 crystals: The as acceptor activity. *Appl. Phys. Lett.* **109**, 172104 (2016).
48. A.J.A. Konings, A.M. van Doormen, D.C. Koningsberger, V.H.J. De Beer, A.L. Farragher, and G.C.A. Schuit: ESR studies on hydrodesulfurization catalysts: Supported and unsupported sulfided molybdenum and tungsten catalysts. *J. Catal.* **54**, 1 (1978).
49. K.C. Khulbe, R.S. Mann, and M. Ternan: Electron spin resonance of the surface chemistry of molybdenum-alumina catalysts, CAN. *J. Chem.* **56**, 1769 (1978).
50. A. Sobczynski and W. Zmierczak: Characterization of MoS_2/SiO_2 by ESR and no absorption. *React. Kinet. Catal. Lett.* **44**, 511 (1991).

Supplementary Material

To view supplementary material for this article, please visit https://doi.org/10.1557/jmr.2018.149.

https://doi.org/10.1557/jmr.2018.149 Published online by Cambridge University Press